Kufa Journal of Engineering
Vol. 17, No. 3, July 2026, P.P. 201-225
Article history: Received 15 June 2025, last revised 23 August 2025,
accepted 31 August 2025

EFFECTS OF HEMATOCRIT VARIATION ON BLOOD FLOW IN A SEGMENT WITH ANEURYSM OF THE POSTERIOR CEREBRAL ARTERY

Chris Naguib[1], Amr Guaily[2,3], Moustafa Elhagri[4], Ahmed Elakhdar[5], Mohammed A. Boraey [6,7], and Mohamed Elshabrawy [8,9]

[1] Smart Engineering Systems Research Center (Sesc), Nile University, Sheikh Zayed District, Giza, 12588, Egypt, Email:c.robert@nu.edu.eg.

[2] Smart Engineering Systems Research Center (Sesc), Nile University, Sheikh Zayed District, Giza, 12588, Egypt, Email:aguaily@nu.edu.eg.

[3] Mechanical Engineering Program, School of Engineering And Applied Sciences, Nile University, Egypt Email:aguaily@nu.edu.eg.

[4] Smart Engineering Systems Research Center (Sesc), Nile University, Sheikh Zayed District, Giza, 12588, Egypt, Email:m.elhagri@nu.edu.eg.

[5] Smart Engineering Systems Research Center (Sesc), Nile University, Sheikh Zayed District, Giza, 12588, Egypt, Email:ah.mohamed@nu.edu.eg.

[6] Mechanical Power Engineering Department, Zagazig University, Zagazig, 44519, Egypt.

[7] Mechanical Engineering Program, School of Engineering and Applied Sciences, Nile University, Egypt, Email:boraey@ualberta.ca.

[8] Engineering Mathematics and Physics Department, Faculty of Engineering, Cairo University, Egypt.

[9] Smart Engineering Systems Research Center (Sesc), Nile University, Sheikh Zayed District, Giza, 12588, Egypt, Email:mmshabrawy@nu.edu.eg.

https://doi.org/10.30572/2018/KJE/170312

ABSTRACT

This article provides a full numerical analysis of blood flow dynamics in a major vascular segment from the lateral surface of the cerebral peduncle to the posterior edge of the midbrain (P2P), which possessed an aneurysm that was identified at a point of bifurcation. In order to realistically model the non-Newtonian behavior of blood, with particular emphasis on its shear-thinning nature, the modified Krieger model 5 (MKM5) was utilized with physiologically realistic parameters. As it is not possible to have inflow data directly for the P2P segment, inlet flow waveform was reconstituted by employing the closest available pulsatile profile of the

basilar artery.The results indicate that standard Carreau and basic Newtonian models are unable to adequately model the hemodynamic response in this complex geometry, but an approximation by a shear-rate-dependent Newtonian model, scaled to the local environment of shear rates, can achieve the accuracy of the more advanced MKM5 model. This result provides a possible simplification to computational fluid dynamics (CFD) simulations in similar research, which might reduce computer expenses without compromising predictive accuracy. These results enable patient-specific modeling strategies in cerebrovascular hemodynamics with specific emphasis on regions of high anatomical complexity and pathologic relevance.

KEYWORDS

Blood Flow, Posterior Cerebral Artery, Aneurysm, Shear Thinning, Hematocrit Variation.

1. INTRODUCTION

Since the inception of its implementation in medical applications, computational fluid dynamics (CFD) has proven to be a powerful tool with prospects for its development and integration in current medical equipment (Mohammed, Kareem, and Mohammed 2022, Onoroh et al., 2023). Cardiovascular diseases (CVDs) are the leading cause of death globally, surpassing more grievous phenomena such as cancer and car accidents. In 2019, approximately 17.9 million people died from CVDs, accounting for 32% of the total deaths globally (Cherry and Eaton 2013).

Aneurysms are ubiquitous forms of anomalies within the vascular system. Specifically, an intracranial aneurysm, i.e., one that occurs inside the brain, is initiated due to feeble cerebral artery walls that consequently promote local expansion in the diseased vessel. Eventually, the arterial walls are thinned by the incessant impulses of the blood against the walls, thereby leading to a balloon-shaped expansion. Saccular aneurysms, in which the balloon creates a sac or berry shape, represent 80%–90% of all brain aneurysms. Aneurysms commonly exist in the bifurcations of large arteries near the Circle of Willis. In addition, they are found in the posterior and anterior circulations. Elhanafy et al. 2019 asserted that 2% of the general populace experienced the development of a saccular aneurysm, and approximately 15 % of the aneurysms occur in the posterior circulation. They also added that 15%–25% of patients developed more than one aneurysm. Saccular aneurysms can lead to subarachnoid hemorrhage (SAH), in which the blood leaks around the brain when the aneurysm ruptures owing to provoked pressure. The annual risk of hemorrhage is estimated at 2%, assuming an incidence of SAH of 10 per 100,000 per year (Elhanafy et al. 2019). About 70% of patients with spontaneous SAH were found to have an aneurysm upon diagnosis, which confirms that saccular aneurysms are the most common cause of nontraumatic SAH (Elakhdar et al. 2021, Elhanafy et al. 2019).

Blood is a complex fluid with different physical properties compared with Newtonian fluids such as water and air (Zhou et al. 2020). Unlike Newtonian fluids, blood comprises a collection of specialized red blood cells (RBCs), white blood cells, and platelets suspended in a light-yellowish liquid that mainly comprises water called plasma. Having a complex composition of liquid and suspended solids, blood viscosity depends on the shear rate. Fluids with such properties are classified as non-Newtonian fluids (Xiang et al. 2011). Because blood viscosity is inversely proportional to the shear rate, blood is classified as a shear-thinning fluid. In addition, due to suspended solids in its composition, blood exhibits elastic characteristics during deformation, leading to the classification of blood as a viscoelastic fluid. Elhanafy et al. 2020

and Geers et al. 2017 considered two-dimensional (2D) axisymmetric geometry for an arterial segment, treated the blood as a viscoelastic shear-thinning fluid, and concluded that the shear-thinning property is markedly more important than the viscoelastic property.

According to previous studies (Hund et al. 2017, Issakhov and Abylkassymova 2023b, Kuchumov et al. 2022), three major weak points are not widely considered during the CFD modeling and simulation processes of the three-dimensional (3D) circulatory system: (1) the non-Newtonian nature of blood is usually not implied for simplification or computational reasons, (2) the unrealistic outlet boundary conditions of the CFD simulation, and (3) the geometry of the vessel not being reflected appropriately. Hence, it was decided to consider these three weak points in the research to provide relatable results that can be used in the future.

According to Lo et al. (2022), the assumption of modeling blood as a Newtonian fluid is incorrect if the main goal is accuracy. Furthermore, blood is not just non-Newtonian fluid; it is a pseudoplastic fluid. Blood viscosity depends on several factors and parameters; the most important ones are plasma viscosity, hematocrit concentration, RBC aggregability, and deformability. As a form of clarification, Lo et al. (2022) explained that blood is less like water and more like toothpaste from the viewpoint of viscosity and material behavior (i.e., the higher the velocity gradient, the smoother the flow and vice versa).

Regarding the boundary conditions to be used for the presented problem, Luo et al. (2011) explained that the use of the "zero-pressure outlet" boundary conditions was a common point in several papers, but according to Moon et al. 2014, the use of this boundary condition provides inaccurate results because this specific type assumes that the vessel is cut and exposed to atmospheric air conditions (which is not a real nor accurate assumption) and thus neglects the change in pressure and flow rate produced by the wave reflection from downstream vessels. In addition, because this wave reflection can be used in CVD diagnosis in the actual field of applied medicine (Ostrowski and Tan 2022, Sakariassen et al. 2015, Hassan, Ahmed, , Mahdi 2014, and Hawary et al 2021), this is a vital point to consider during the modeling of blood flow simulation. Moon et al. 2014 suggested that the use of "impedance" applied at the outlet boundary conditions is a better path toward achieving an accurate result. This point was also proven by Luo et al. 2011. The hemodynamic conditions at the outlets were depicted using the Windkessel model. The Windkessel model is a circuit analogy of human vasculature. Windkessel can model the outlet boundary conditions by proximal resistance connected in series with a capacitor parallel to the distal resistance (RCR) model or by proximal resistance connected in series with a capacitor (RC) model. The latter was adopted in this paper.

2. METHODOLOGY

2.1. Geometry of the artery

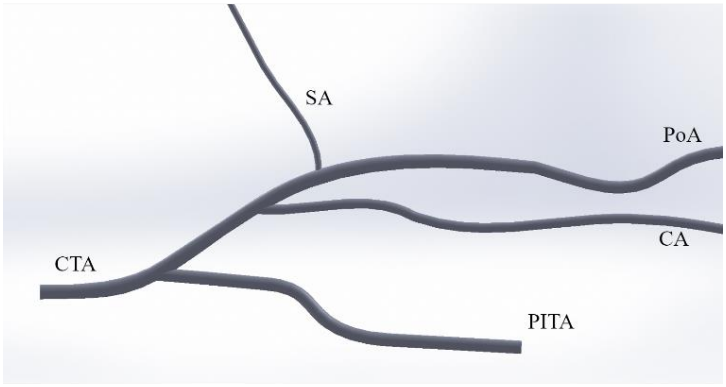

Fig. 1. P2P segment of the posterior cerebral artery. The figure shows the CTA inlet, PITA outlet 1, CA outlet 2, SA outlet 3, and poa outlet 4. CTA, common temporal artery; PITA, posterior inferior temporal artery; CA, calcarine artery; SA, splenial artery; poa, parieto-occipital artery

This paper explores the P2P segment of the posterior cerebral artery (PCA). The 3D model is depicted based on a 2D schematic, illustrated in Fig. 1 (Salvi et al. 2013) This segment provides blood supplies to the occipital lobe (responsible for vision) and posteromedial temporal lobes involved in processing sensory input. The aneurysm was located at the posterior inferior temporal artery (PITA) bifurcation point. It has a maximum expansion diameter of $2.39\ mm$ and an extension from the primary bifurcation point of $2.44\ mm$ (Shimogonya and Fukuda 2024).

2.2. Rheological models

Blood viscosity is complex; thus, several rheological models were investigated to accurately describe blood viscosity. The simplest case is considering blood a Newtonian fluid with a constant dynamic viscosity of $0.0035\ Pa\ s$.

To approximate the shear thinning nature of the blood, the Carreau model was applied. Carreau fluid bases the viscosity on the shear rate; it behaves as a Newtonian fluid at a low shear rate and as a power law fluid at a high shear rate. Eq. 1 represents the mathematical formulation of the Carreau model (Vignon-Clementel et al. 2010). The Carreau model is built in the ANSYS Fluent and only requires the values for the constants relevant to the blood properties.

$$\mu = \mu_\infty + (\mu_0 - \mu_\infty)(1 + A|\dot{\gamma}|^2)^m \qquad (1)$$

Where $A = 10.976, m = -0.3216, \mu_\infty = 0.0035\ Pa.s, \mu_0 = 0.056\ Pa.s$

where μ_∞ is the viscosity at the infinite shear rate, μ_0 is the zero-shear rate viscosity, A, n are constant, and $\dot{\gamma}$ is the shear rate. To advance one step, we implemented a model that simulates and manifests the actual nature of the blood by considering hematocrit concentration; thus, we eventually adopted the MKM5 model. The general form of the model is as follows:

$$\eta = \eta_{pl} \times (1 - \frac{HCT}{HCT_{critical}})^{-n} \quad (2)$$

where η_{pl} is the plasma viscosity taken as $1.23\,CP$ for healthy people, and HCT is the concentration of hematocrit in the blood. Furthermore, the $HCT_{critical}$ is the concentration of the hematocrit at which the blood refuses to act as a liquid and acts like a solid, which is at approximately 98% or 99%. The exponent n monitors the shear-thinning aspect of the blood governed by the disaggregation of RBCs.

Here, n acts as a piecewise function depending on the hematocrit concentration in the blood. The general form is as follows:

$n = n_\infty$ when $HCT < HCT_{ST}$

$n = n_\infty + n_{st}$ when $HCT > HCT_{ST}$

where $n_\infty = a + b \times e^{-c \times HCT}$, $n_{st} = \beta \times \gamma'^{-v}$, $\gamma' = 1 + (\lambda \times \gamma)^v$

Note that γ' is the nondimensional shear rate, n_{st} is the shear-thinning component, and HCT_{ST} is a threshold where shear thinning is not observed.

The parameters for the MKM5 model were taken from (Vignali et al., 2021) and are listed in Table 1; a sensitivity analysis of these parameters was not conducted and represents a valuable direction for future work.

Table 1. Modified Krieger model 5 parameter values

Model parameter	*a*	*b*	*c*	*β*	*λ*	*v*
MKM5	0	8.71	2.87	8.23	108	0.134

While the velocity itself is not included explicitly in Eq.2, the effect of flow velocity is represented by the velocity gradient through the exponent *n*. The MKM5 model offers substantial improvement over blood modeling, such as a Newtonian fluid or the Carreau model by including hemodynamic and microstructural intricacies. In contrast with the Newtonian assumption (fixed viscosity), MKM5 considers shear-thinning, which closely resembles blood's actual-world rheology. Although the Carreau model includes shear-dependent viscosity, MKM5 further incorporates cell deformation, aggregation, and microcirculatory impacts, allowing for more precise simulation in narrow vessels and pathological flow conditions. The MKM5 model is not readily available in ANSYS Fluent; thus, it was introduced to ANSYS Fluent as a programmed user-defined function (UDF) file.

2.3. Boundary conditions

Inlet: To efficiently simulate blood flow, an inlet mass flow rate function must be used as the inlet boundary condition inside ANSYS as a UDF. The presence of such a direct function at the inlet of specific arteries is rare in the literature; however, graphs are more common. Using the free software WebPlotDigitizer, reported mass flow rate graphs in the literature were discretized

to extract discrete data representing the variable of interest (velocity, volume flow rate, etc.) against time. Next, discrete data points were loaded into MATLAB, and the curve-fitting application was used to generate the Fourier series describing function based on the input data. After matching the resulting function against the actual input data, this function is finally implemented as a C code representing the UDF to be imported to ANSYS as the inlet boundary condition.

The medical literature lacks an exact mass flow rate for the cerebral segment present in this study. Thus, the Re number at the inlet of the model is evaluated through a simple parametric study by comparing the flow characteristics—especially maximum flow velocity—at three different Re numbers: $50, 100, and\ 200$. Three steady-state Newtonian simulations at the healthy geometry model were performed with the inlet mass flow rates: 9.474×10^{-4}, $4.9431 \times, and\ 9.86 \times 10^{-4}\ kg/s$ for the aforementioned Re numbers, respectively. The flow patterns for all simulations were physically valid in terms of the patterns; however, the maximum velocity was the decisive factor in the medical literature. The maximum velocities were $18.9, 34.9,$ and $68.3\ cm/s$, as shown in Figs. 2, 3, and 4, respectively, for the three Re numbers. Vu et al. (2025) reported a mean blood flow velocity of $41.2\ (\pm 8.6)\ cm/s$ (mean ± standard deviation) in the left PCA that favors the case of $Re = 100$ with a max velocity of $34.9\ cm/s$, which seems acceptable because the pulsatile flow will magnify the flow velocity across the whole fluid domain.

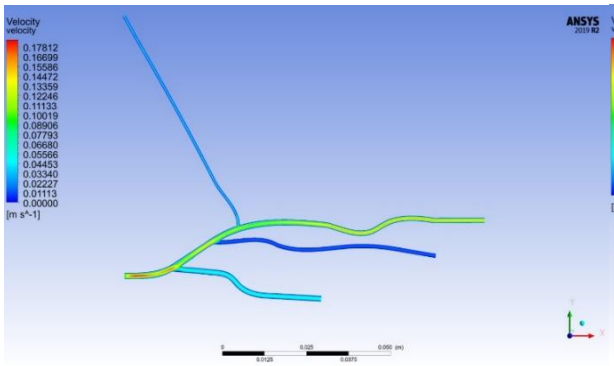

Fig. 2. Velocity contour of the P2P segment at $Re = 50$

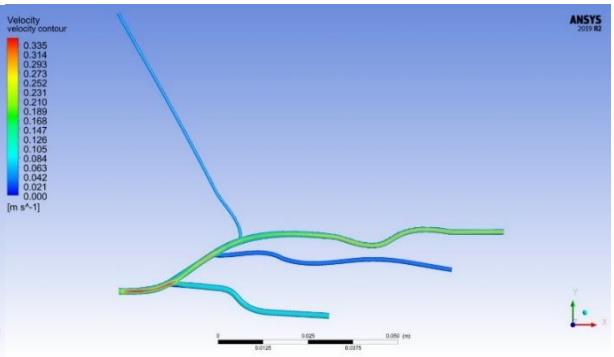

Fig.3. Velocity contour of P2P segment at $Re = 100$

Because the blood flow pulse at the exact inlet in this study is unavailable in the literature, it is deduced with respect to the closest available pulse, the basilar artery (BA) pulse. Wajihah and Sankar 2023 reported a volume flow rate pulse in the BA, which directly feeds the PCA. We assumed that the pulse at the inlet has the same features but scaled down, considering the mass flow rate values. Fig. 5 represents the fitted function against the actual data.

It is worth noting that the use of a scaled BA waveform is acknowledged as a primary limitation

of this study. Direct flow measurements in the P2P segment are rare in clinical literature due to the invasiveness and technical challenges of obtaining such data. Therefore, employing a scaled waveform from a proximal, feeding artery is a necessary pragmatic approach in computational hemodynamics (Cebral et al. 2005) and (Sforza et al. 2009). The key assumption is that the pulsatile characteristics (shape, period, harmonics) are preserved from the BA to the PCA, while the amplitude is scaled based on the reduction in vessel diameter and flow division.

The main impact of this assumption is on the absolute values of hemodynamic parameters, most notably the Wall Shear Stress (WSS) and velocity magnitudes, which scale approximately linearly with the flow rate. However, the primary objective of this study was a comparative analysis of the relative effects of different rheological models and hematocrit levels under identical inflow conditions. Since the same inlet waveform was used across all simulations, the trends and conclusions regarding the influence of hematocrit and model choice are robust and internally valid. The finding that a shear-rate- informed Newtonian model can approximate the MKM5 results, for example, is independent of the absolute flow rate.

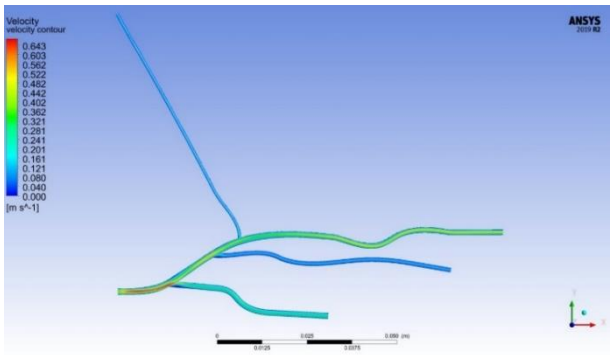

Fig. 2. Velocity contour of the P2P segment at Re = 200

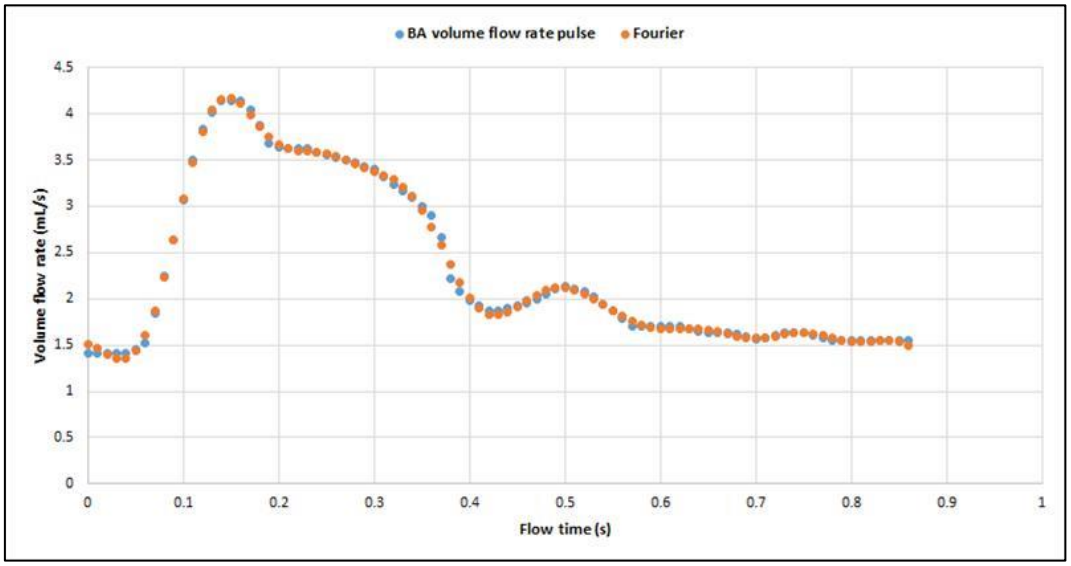

Fig. 3. Comparison between original pulse and curve-fitted pulse using 8 Fourier terms and period of 0.8567 seconds. BA, basilar artery

The resulting mass flow rate pulse of BA is as follows:

$$\dot{m}(t) = 1050 * 10^{-6} * [2.333 + B_1\, cos(xt) + A_1\, sin(xt) + B_2\, cos(2xt) + A_2\, sin(2xt) + B_3\, cos(3xt) + A_3\, sin(3xt) + B_4\, cos(4xt) + A_4\, sin(4xt) + B_5\, cos(5xt) + A_5\, sin(5xt) + B_6\, cos(6xt) + A_6\, sin(6xt) + B_7\, cos(7xt) + A_7\, sin(7xt) + B_8\, cos(8xt) + A_8\, sin(8xt)]\ kg/s \quad (3)$$

To compare the flow rate at the BA with that at the inlet, the following integral is performed to obtain the average steady flow rate of the BA:

$$\dot{m}_{avg} = \frac{\int_0^{0.8567} \dot{m}(t)dt}{0.8567} = 2.4513 \times 10^{-3}\ kg/s \quad (4)$$

Comparing the average mass flow rate at the BA with that of the inlet at $Re = 100$ results in the reduction factor of the pulse:

$$f = \frac{4.9431 \times 10^{-4}}{2.4513 \times 10^{-3}} = 0.2017 \quad (5)$$

Thus, the final mass flow rate pulse at the inlet is as follows:

$$\dot{m}(t) = 0.2017 * 1050 * 10^{-6} * [2.333 + B_1\, cos(xt) + A_1\, sin(xt) + B_2\, cos(2xt) + A_2\, sin(2xt) + B_3\, cos(3xt) + A_3\, sin(3xt) + B_4\, cos(4xt) + A_4\, sin(4xt) + B_5\, cos(5xt) + A_5\, sin(5xt) + B_6\, cos(6xt) + A_6\, sin(6xt) + B_7\, cos(7xt) + A_7\, sin(7xt) + B_8\, cos(8xt) + A_8\, sin(8xt)]\ kg/s \quad (6)$$

Where sine and cosine coefficients of Fourier series obtained by $A_n = \frac{2}{T}\int_0^T f(t)\, sin(nxt)\, dt$, $B_n = \frac{2}{T}\int_0^T f(t)\cos(nxt)$, $n \geq 1$. Table 2 illustrates the values of the abovementioned symbols. The coefficients are calculated from an individual flow-time dataset and thus are specific to that waveform. They have different values in arteries such as the basilar or femoral because of different hemodynamics. They also have different values in different people and in the same person under different states, for example, rest versus exercise or health versus disease, because of changes in physiology and pathology

Table 2. Values of symbols used in equations 3 and 6

Symbol	x	B_1	A_1	B_2	A_2	B_3	A_3	B_4	A_4
Value	7.334	0.2172	1.029	0.5348	0.07737	0.1462	0.143	0.2025	0.1423
Symbol	B_5	A_5	B_6	A_6	B_7	A_7	B_8	A_8	
Value	0.1126	0.1974	0.0472	0.02882	0.0972	0.00611	0.02489	0.04064	

Outlet: For the modeled arteries, data that describe the flow parameters at the outlets is insufficient. Therefore, an outflow boundary condition was used. The manual of ANSYS Fluent describes its use for the outflow boundary conditions to model flow exits where the details of the flow velocity and pressure are unknown before solving the flow problem. In addition, Fluent requires the allocation of flow rate ratios if used for more than one outlet. Because such medical data are unavailable for the P2P segment of PCA, the RC Windkessel model was used in this

study to systematically account for the outlet flow rate ratios while attempting to capture the realistic properties of the arteries.

From the work of Weber et al. 2004, the formula provided below was used to calculate the mass flow rate ratio between the two branches of a bifurcation for steady flows:

$$\frac{Q_1}{Q_2} = \frac{L_2K_2 - R_2}{L_1K_1 - R_1}, \tag{7}$$

where L is the length of each branch, and R represents the distal resistance of small arterioles and capillaries to blood flow. K_1 and K_2 are evaluated from the following equation:

$$K = \frac{-8}{\pi r^4 Re}, \tag{8}$$

where Re is the Reynolds number. In the realistic case of pulsatile flow, the following relation was used:

$$\frac{Q_{1,k}}{Q_{2,k}} = \frac{L_2 + \frac{i}{\omega_k}\gamma_2 - \frac{R_2R_2C_2}{1 + i\omega_k R_2C_2}}{L_1 + \frac{i}{\omega_k}\gamma_1 - \frac{R_1R_1C_1}{1 + i\omega_k R_1C_1}}, \tag{9}$$

where

$$\gamma_j = L_jK_j - R_j \tag{10}$$

Note that i is the imaginary number and ω_k is the Fourier frequency of the pulse. However, the resistance R_i and capacitance C_i at the outlets are unknown. Hence, the values provided in the study by Wajihah and Sankar 2023 were used in this study. There were no data for the resistances and capacitances of the exact arteries present in this study; thus, the data for the closest artery (in spatial proximity) in the cerebral vasculature were assumed for all outlets ($R = 83.8 \times 10^8\ N\,S/m^5$) ($C = 5.41 \times 10^{-11}\ m^5/N$). The closest artery found in the work of Wajihah and Sankar 2023 was the left PCA, which provides the blood supply for the P2P segment that constitutes the modeled arteries in the present study.

Table 3 illustrates the dimensions of the outlets plotted in Fig. 3. These dimensions are used later in the flow rate ratio calculations. The lengths of outlets Q_1, Q_3, Q_5, and Q_6 are extended by 10 times their diameters to accommodate the outflow boundary condition to prevent forcing the flow to the fully developed behavior.

The geometry can be approximated as a series of (Y-shaped) bifurcations. This means that the inlet is bifurcated into Q_1, Q_2; then Q_2 forms another (Y-shaped) bifurcation into Q_3 and Q_4; finally, Q_4 forms another (Y-shaped) bifurcation into Q_6 and Q_5. The dimensions from Table 3 are substituted into Eqs. 5 and 6 at the three Re $(50, 100, \text{and } 200)$ to evaluate the flow rate ratios at each bifurcation. Then, the flow rates are evaluated at the outlets $(Q_1, Q_3, Q_5, \text{and } Q_6)$ as a ratio from the main flow rate at the inlet according to Fig. 7.

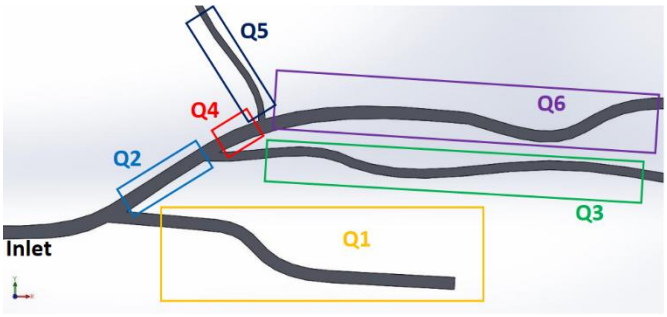

Fig. 6. Locations of the outlets of posterior cerebral artery with outlet code names

Table 3. Posterior cerebral artery outlet dimensions

	Q_1	Q_2	Q_3	Q_4	Q_5	Q_6
$L\ (mm)$	46.76	14.34	65.94	8.81	71.27	74.83
$r\ (mm)$	0.8	0.81	0.6	0.9	0.4	0.75

$$\frac{Q_1}{Q_2} = B1,\ \frac{Q_3}{Q_4} = B2,\ \frac{Q_6}{Q_5} = B3$$

$Q_1 + Q_2 = 1$	$Q_3 + Q_4 = Q_2$	$Q_6 + Q_5 = Q_4$
$B1 \times Q_2 + Q_2 = 1$	$B2 \times Q_4 + Q_4 = Q_2$	$B3 \times Q_5 + Q_5 = Q_4$
$Q_2 = \frac{1}{(1+B1)}$	$Q_4 = \frac{Q_2}{(1+B2)}$	$Q_5 = \frac{Q_4}{(1+B3)}$
$Q_1 = 1 - Q_2$	$Q_3 = B2 \times Q_4$	$Q_6 = B3 \times Q_5$

Fig. 7. Calculation of outlet flow rates as ratios from the inlet

Table 4 summarizes the flow rate ratios of the outlets used in Newtonian steady simulations at each outlet with respect to each inlet Re.

Table 4. Outlet flow rate ratios of the inlet at each Re for the Newtonian steady flow

	$Re = 50$	$Re = 100$	$Re = 200$
Q_1 (PITA)	0.276	0.311	0.3552
Q_3 (CA)	0.039	0.054	0.0782
Q_5 (SA)	0.057	0.055	0.0543
Q_6 (PoA)	0.628	0.580	0.5123

PITA, posterior inferior temporal artery; CA, calcarine artery; SA, splenial artery; PoA, parieto-occipital artery

2.4. Steady-state shear-thinning models

Because the above models were designed for Newtonian fluids, we need to account for the shear-thinning property of blood. The change in blood properties is reflected indirectly in Eq.8 of the K parameter typically at the value of the Re. Thus, R_e is recalculated for the different shear-thinning models—Carreau and MKM5—and resubstituted in Eq. 8 to reassess the outlet flow ratios. Re number is calculated from the formula $R_e = \frac{\rho v D}{\mu}$; moreover, the blood density is constant at 1050 kg/m^3 and the inlet diameter (D) is constant at 1.8 mm, in addition to the

same flow velocity at the inlet of 0.093, 0.185, and 0.37 m/s for the inlet's three Re numbers of 50, 100, and 200, respectively. The only change appears in the viscosity value according to each model. The average viscosity value was calculated for each model using a MATLAB script that runs the models' equations for a shear rate range of 1-2000 s^{-1}, as reported by (Elhanafy et al. 2019). The average viscosities considered were 0.003985 Pa.s and 0.0072 Pa.s for the Carreau and MKM5 models, respectively. After that, R_e was recalculated. The flow rate ratios at each outlet were recalculated using the same procedure described above. Table 5 summarizes the flow rate ratios of the outlets used in the shear-thinning steady simulations at each outlet with respect to each inlet Re.

Table 5. Outlet flow rate ratios of the inlet at each Re for the shear thinning steady flow

	Carreau Steady			MKM5 Steady		
Inlet Re	$Re = 50$	$Re = 100$	$Re = 200$	$Re = 50$	$Re = 100$	$Re = 200$
Q_1 (PITA)	**0.271**	**0.303**	**0.346**	**0.2528**	**0.275**	**0.3088**
Q_3 (CA)	**0.037**	**0.051**	**0.073**	**0.0298**	**0.038**	**0.0535**
Q_5 (SA)	**0.057**	**0.056**	**0.055**	**0.0578**	**0.057**	**0.0555**
Q_6 (PoA)	**0.635**	**0.590**	**0.526**	**0.6596**	**0.630**	**0.5822**

The flow rate ratios for pulsatile flow were calculated using Eq.9. Note that the flow rate is a function of the Fourier frequency. Thus, the flow rate at each outlet was averaged for the 8 Fourier frequencies used to simulate the inlet pulse. Two methods were used to calculate the weighted average and tested against the medical literature for the carotid bifurcation flow rate ratios to determine the most accurate method.

3. RESULTS

First, $B_{n,k}$ were calculated for the two branches for all k values as previously done, resulting in an imaginary number. After that, we calculated the ratio $\frac{Q_{1,k}}{Q_{2,k}}$ according to Eq. (7). Then, the ratio $\frac{Q_{1,k}}{Q_{2,k}}$ was converted to a real number according to:

$$\left(\frac{Q_{1,k}}{Q_{2,k}}\right)_{Real} = \sqrt{\left[\left(\frac{Q_{1,k}}{Q_{2,k}}\right)_{complex} \times \left(\frac{Q_{1,k}}{Q_{2,k}}\right)_{conjugate}\right]} \tag{11}$$

For each Fourier frequency of the pulse, $\omega_k = kx$, $(k = 1, \ldots 8)$, the corresponding periodic time T_k is calculated as $T_k = 2\pi/\omega_k$, then fractional duration T_k^f is calculated by dividing T_k by the total bold flow cycle time which is 0.8567 s for cerebral position. The weighted average of each frequency is calculated by:

$$\left(\frac{Q_{1,k}}{Q_{2,k}}\right)_{weighted} = \left(\sqrt{\left[\left(\frac{Q_{1,k}}{Q_{2,k}}\right)_{complex} \times \left(\frac{Q_{1,k}}{Q_{2,k}}\right)_{conjugate}\right]}\right) \times T_k^f \tag{12}$$

Then, all weighted average ratios were summed to obtain the final equivalent ratio:

$$\frac{Q_1}{Q_2} = y = \sum_{k=1}^{8} \left(\frac{Q_{1,k}}{Q_{2,k}}\right)_{weighted} \quad (13)$$

Finally, simple algebra was used to calculate the flow rate of each branch as a ratio to the inlet flow rate in the following manner:

$$Q_1 + Q_2 = 1 = y \times Q_2 + Q_2 \quad (14)$$

$$Q_2 = \frac{1}{(1+y)} \quad (15)$$

Table 6 compares the results of methods I and II with the carotid bifurcation ratios from the medical literature. It was found that method II is far closer to the real-life results.

Table 6. Carotid bifurcation flow rate ratios

	Method I	Method II	Hoi et al. 2010	Marshall et al 2004
Q_1(ICA)	**0.44**	**0.68**	**0.63**	**0.7**
Q_2(ECA)	**0.56**	**0.32**	**0.32**	**0.26**

Because the second method has been proven to be accurate in the medical literature, it was applied for cerebral bifurcations. The effect of shear thinning was accounted for through the Re by averaging the viscosity, as discussed above.

Table 7 summarizes the flow rate ratios of the outlets at each outlet for inlet $Re = 100$ for transient simulations with various viscosity models.

Table 7. Cerebral segment outlet flow rate ratios for various transient viscosity models

	Newtonian	Carreau Steady	MKM5
Inlet Re	$Re = 100$	$Re = 100$	$Re = 100$
Q_1 (PITA)	**0.524**	**0.5156**	**0.487**
Q_3 (CA)	**0.074**	**0.0704**	**0.057**
Q_5 (SA)	**0.013**	**0.0134**	**0.014**
Q_6 (PoA)	**0.389**	**0.4006**	**0.442**

3.1. P2P segment of PCA Results

To check the mesh independence of our simulation, we attempted 8 different meshes with a varying number of elements to reach the optimum mesh within the present constraints of our available computational power. To track the quality of each generated mesh, two specific properties were chosen to differentiate between them: aspect ratio and skewness. Both properties were maintained within the safe range of values. In all mesh trials, two factors were changed to produce the different meshes: the global element size and the sphere of influence (SOI) created at the center of each outlet circumference. The following table expresses the eight mesh trials in detail (Shimogonya and Fukuda 2024).

As shown in Fig. 8, describing the variation in average wall shear stress (WSS) with tried number of elements, starting from the fourth mesh (number of elements = 321,968), the change

in average WSS was insignificant and a further increase in the number of elements was unjustified.

Table 8. Summary of mesh trials

Trial #	# of elements	# of nodes	Element size (Global - SOI)	Aspect ratio			Skewness		
				min.	max.	avg.	min.	max.	avg.
1	87,704	139,279	0.4 − 0.24	1.1758	22.564	1.8352	$1.05E-03$	0.93383	0.22793
2	132,486	206,308	0.35 − 0.21	1.1673	17.299	1.8278	$2.42E-04$	0.91998	0.22557
3	210,013	319,264	0.3 − 0.18	1.1634	25.843	1.8187	$1.29E-04$	0.94832	0.22093
4	321,968	479,962	0.27 − 0.15	1.1615	14.869	1.8128	$2.37E-05$	0.99893	0.21823
5	459,309	678,485	0.23 − 0.14	1.1578	11.815	1.8084	$2.01E-07$	0.9233	0.21564
6	671,323	959,995	0.29 − 0.1	1.161	15.48	1.8029	$4.56E-05$	0.99837	0.2149
7	1,040,092	1,481,070	0.22 − 0.09	1.1581	9.6778	1.7976	$2.36E-06$	0.94056	0.21211
8	1,523,997	2,173,141	0.16 − 0.09	1.1582	9.9597	1.7941	$2.79E-06$	0.9318	0.20974

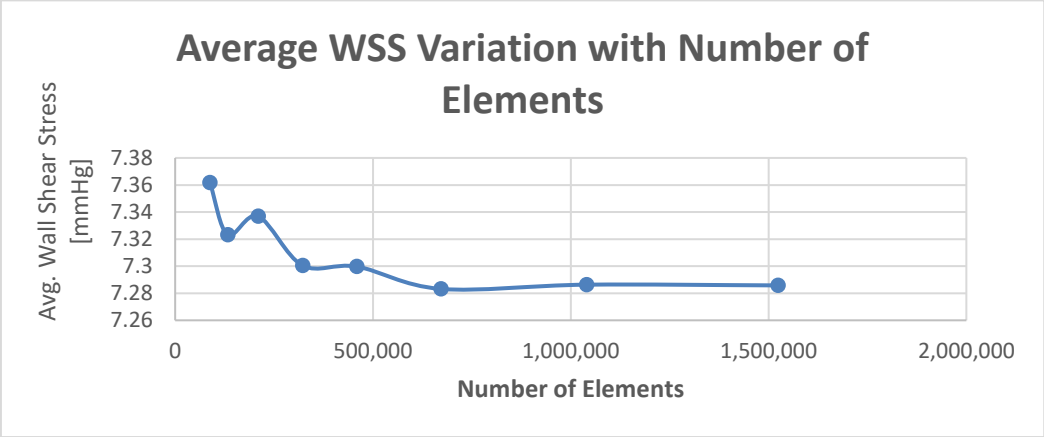

Fig. 8. Average wall shear stress (WSS) variation with number of elements

3.2. P2P segment of PCA results

First, we discuss the effect of variations in hematocrit values on the blood flow field. As shown in Fig. 9, there is a marked amount of deviation in viscosity when considering the hematocrit concentration from the Newtonian value (0.0035 Pa.s).

Second, we discuss the streamlines at peak systole for all simulations. There were no major differences in the flow patterns. A kind of swirl crossing each other occurred inside the aneurysm. Notably, the maximum velocity at the domain increased with the increase in average viscosity, which was mainly due to the fixed period of the pulse; therefore, the fluid had to accelerate to overcome the additional resistance caused by viscosity. The Newtonian value of 0.007477 Pa.s was deduced by weighing the average viscosity throughout the domain at 45% hematocrit, and Fig. 10c represents the streamlines produced after implementing the value. In addition, the boundary layer thickness will increase at higher hematocrit values, and as a result, the effective area will be diminished; therefore, the velocity must increase to accommodate for the decrease in the effective area, as shown in Fig 10a, Fig. 10b, and 10d.

The velocity vectors in Figs. 11a–11d, however, show a small variation in the flow pattern with changes in hematocrit concentration. At 12.6% hematocrit, a circulation zone was noticed at the PITA branching just below the aneurysm. This zone disappeared with an increase in the

hematocrit value, which was equivalent to a decrease in the local Re. This can be attributed to the dominance of viscous forces over inertial forces in this area, which resembles a sudden change in flow area for a pipe flow.

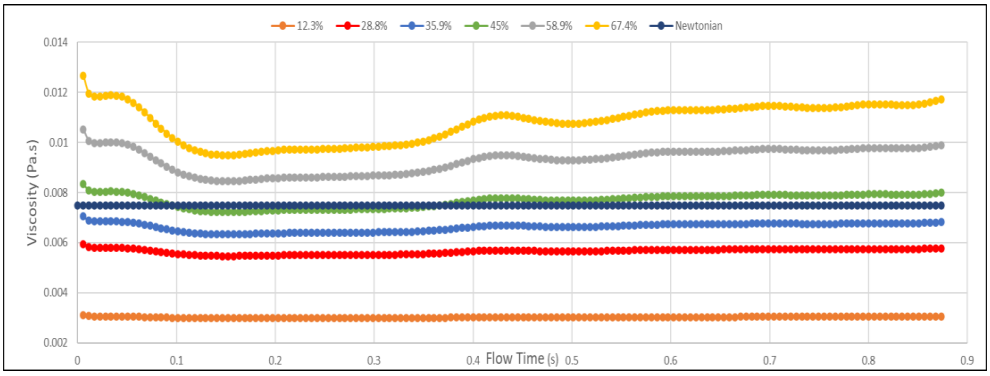

Fig. 9. Area-weighted average viscosity against flow time for various hematocrit concentrations

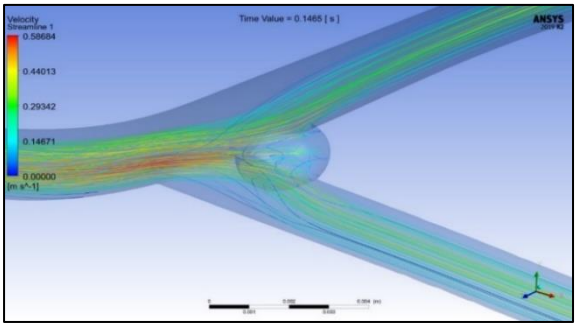

Fig. 10a. Streamlines at peak systole for $hematocrit = 12.3\%$

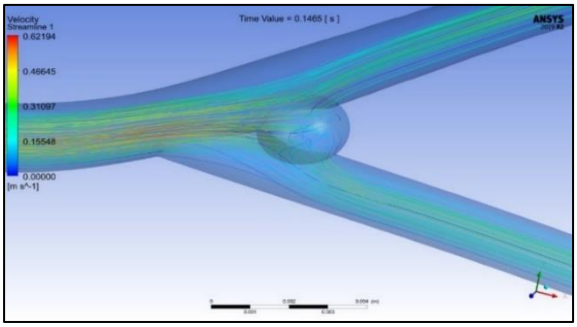

Fig. 10b. Streamlines at peak systole for $hematocrit = 45\%$

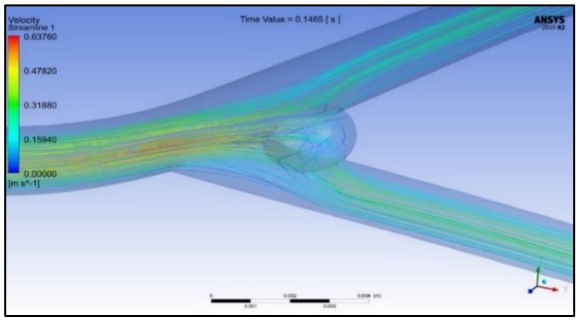

Fig. 10c. Streamlines at peak systole for Newtonain flow with viscosity $0.007477\ Pa.s$

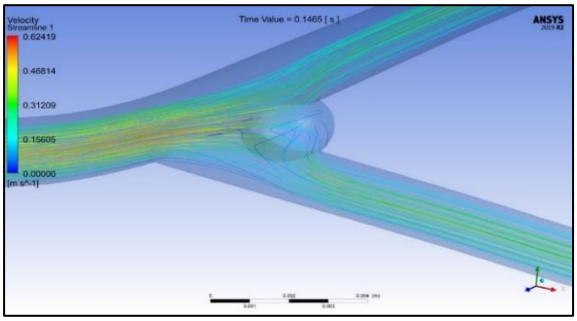

Fig. 10d. Streamlines at peak systole for $hematocrit = 67.4\%$

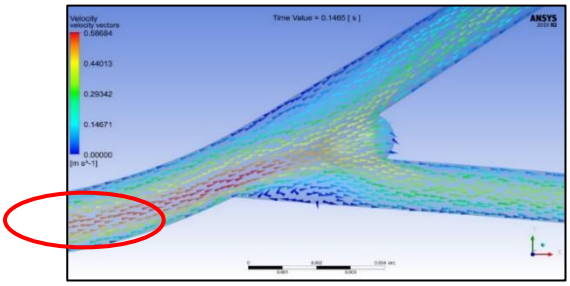

Fig. 11a: Velocity vectors at peak systole flow rate at $hematocrit = 12.3\%$

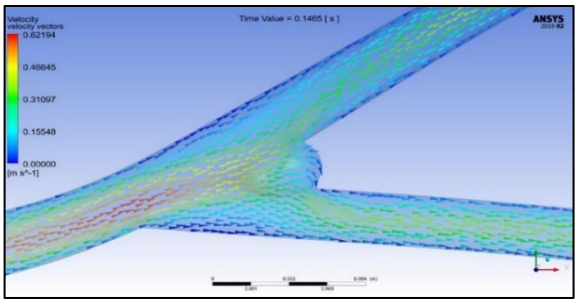

Fig. 11b: Velocity vectors at peak systole flow rate at $hematocrit = 45\%$

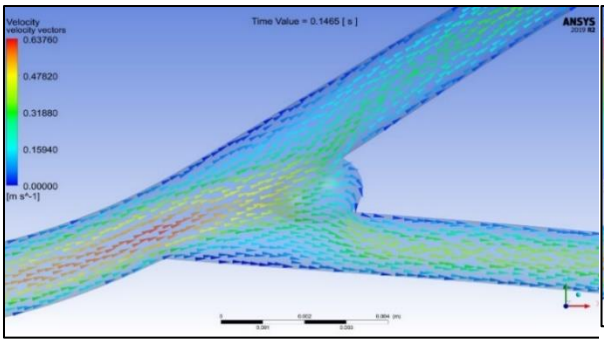

Fig. 11c: Velocity vectors at peak systole Newtonian flow with viscosity $0.007477\ Pa.s$

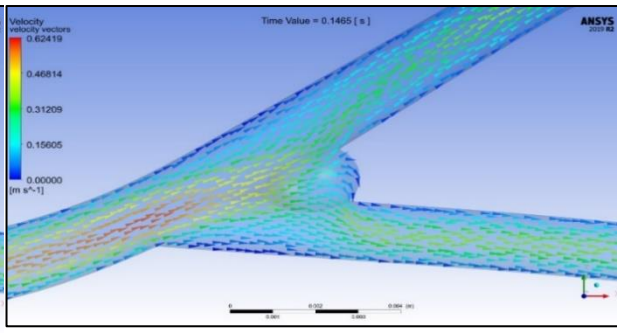

Fig. 11d Velocity vectors at peak systole flow rate at $hematocrit = 67.4\%$

To discuss the differences between the different flow rates from peak systole to the start of diastole on the flow patterns, the average hematocrit value of 45% is chosen as a representative simulation. The pressure contours Fig. 12 show that the pressure difference at peak systole is $17.077\ mmHg$, which is more than double the $7.0878 - mmHg$ value at the start of diastole. This is expected because the higher flow rate at peak systole requires a higher-pressure difference to accommodate the excess flow rate to be delivered. From the streamlines, aggressive swirling and mixing of the streamlines inside the aneurysm was observed, whereas at the start of the diastole, the streamlines seemed more parallel and smoothly flowing, as shown in Figs. 13a and 13b.

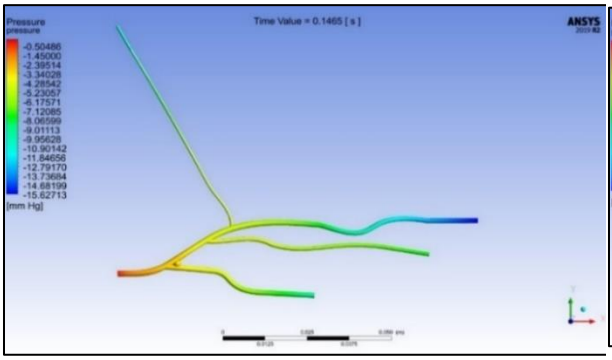

Fig. 12a. Pressure contours for $hematocrit = 45\%$ at peak systole

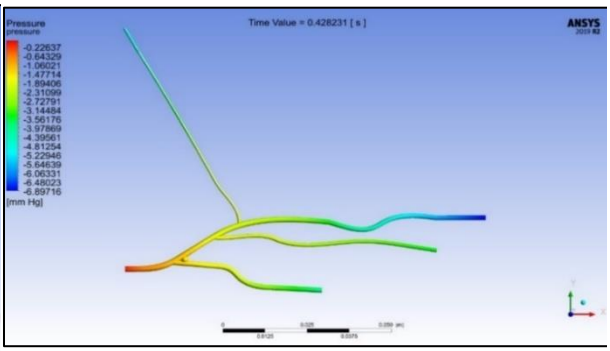

Fig. 12b. Pressure contours for $hematocrit = 45\%$ at start of diastole

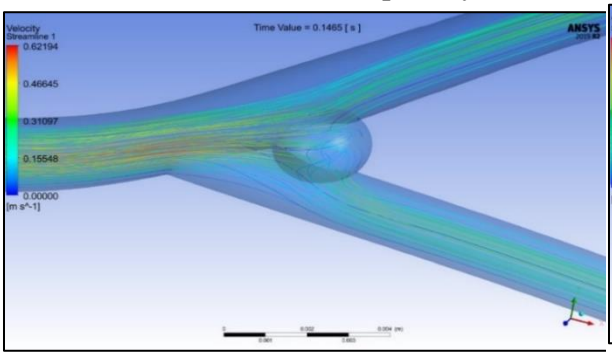

Fig. 13a. Streamlines for $hematocrit = 45\%$ at peak systole

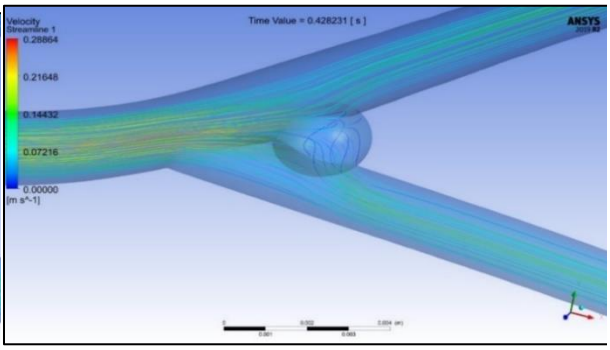

Fig. 13b. Streamlines for $hematocrit = 45\%$ at start of diastole

The WSS stress contours suggested that WSS increased with an increase in flow rate, which was later confirmed. Moreover, the contours showed that the maximum WSS occurred around the aneurysm edges, especially at the aneurysm neck Fig. 14, which is similar to the results of a previous study WHO 2025.

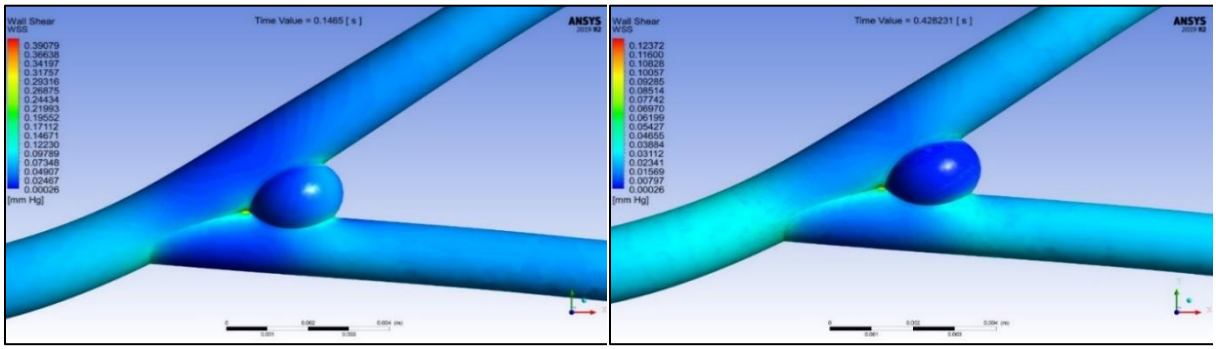

Fig. 14a. Wall shear stress contours for $hematocrit = 45\%$ at peak systole

Fig.14b. Wall shear stress contours for $hematocrit = 45\%$ at start of diastole

3.3. Property graphs

Because it is difficult to observe the flow features using 3D plots, the results are represented using 2D charts in this section. Fig. 15 shows the probe points used for data representation in the following charts. The chart in Fig. 16 represents the inlet mass flow rate pulse, with five red points highlighted. These points represent the time stations used in the charts. Note that not all five time points are used in all charts. Usually, time points at the minimum and maximum flow rates are used.

The first established conclusion is that as the hematocrit value increases, the WSS also increases at all locations, as shown in Fig. 17.

Another important conclusion is observed in Fig. 19 between the wall pressure values and the hematocrit values. Notably, an increase in the hematocrit value causes a decrease in the wall pressure and vice versa, which leads to a higher probability of aneurysm rupture for lower hematocrit values.

The same relations hold on the aneurysm wall, as shown in Fig. 21

To confirm the earlier observation that WSS increases with an increase in flow rate, the WSS was graphed for the five flow rates mentioned previously. Fig. 21 shows that WSS has a direct relationship with the mass flow rate.

It was observed from the pressure graphs that viscosity needs to increase with an increase in the hematocrit value, as it clarifies many things although without proof so far. Fig. 23 provides this proof and shows an increase in average viscosity as the hematocrit value increases. The experimental data in the study by Xiang et al. (2011) supports this trend.

Fig. 24 is vital as it shows that WSS increases with the increase in hematocrit value and, in turn, with the increase in viscosity. Beyond the numerical values, these findings propose a mechanistic insight into aneurysm pathology. Our simulations demonstrate that low hematocrit creates a hemodynamic environment characterized by reduced wall shear stress. Given that low WSS is a well-established driver of inflammatory wall remodeling and aneurysm growth (Meng et al., 2007), this suggests a potential biomechanical link whereby comorbid anemia could contribute to an unstable aneurysm phenotype.

However, as this is a computational study, this asserted link between hematocrit and rupture risk remains hypothetical and must be validated with future epidemiological and clinical studies. If confirmed, these findings would highlight the need for clinicians to consider a patient's hematological profile as part of a comprehensive aneurysm risk assessment.

Fig. 25 compares the WSS between healthy geometry and aneurysmatic geometry. Observably, for the same viscosity model, the resulting WSS is almost identical for both cases. The important finding from this graph is that the behavior and values of Newtonian viscosity are close to the hematocrit model that has the same average viscosity. However, the Carreau and Newtonian models are far from close. Hence, it can be concluded that the Newtonian model can provide results as accurately as those provided by the complicated MKM5 model but for a modified viscosity value based on the local shear rate range.

Souza et al., 2024 studied combined PTV experiments and CFD simulations to look at blood flow in three intracranial aneurysms. Their results showed high WSS at the necks, which indicates a risk of rupture, and increased OSI/RRT in the sacs, suggesting a risk of growth or thrombosis. They observed strong vorticity in transient flows. The PTV-CFD approach offered affordable, patient-specific insights to improve aneurysm management and predict ruptures.

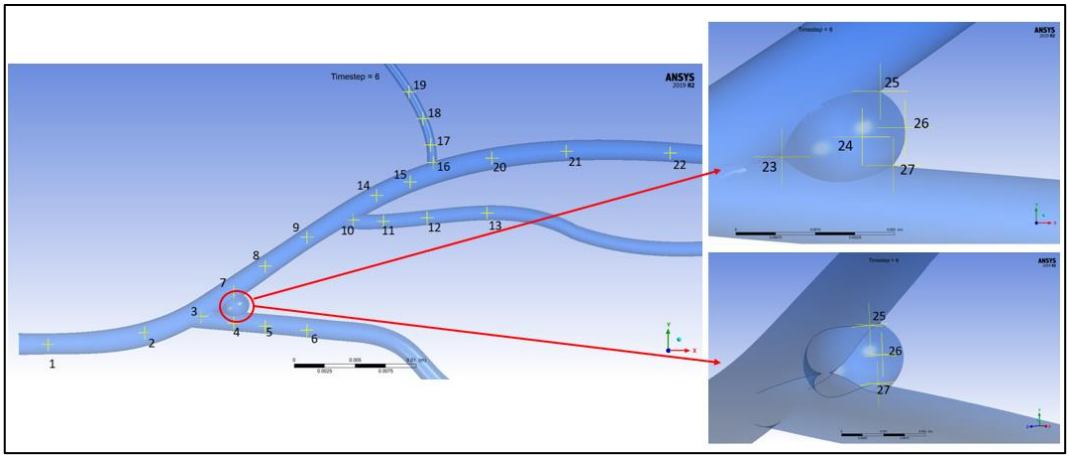

Fig. 15: Probe locations for wall shear stress and wall pressure comparison

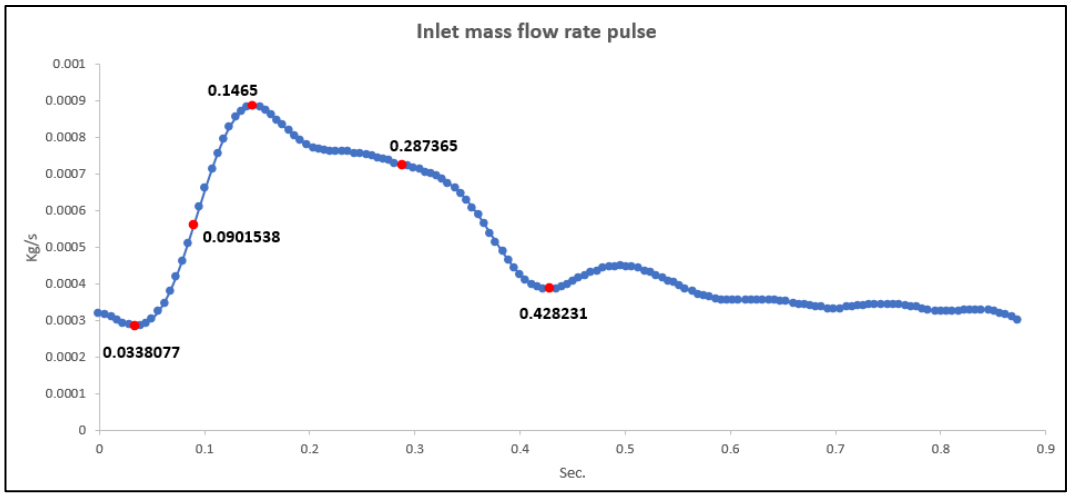

Fig. 16: Inlet mass flow rate pulse

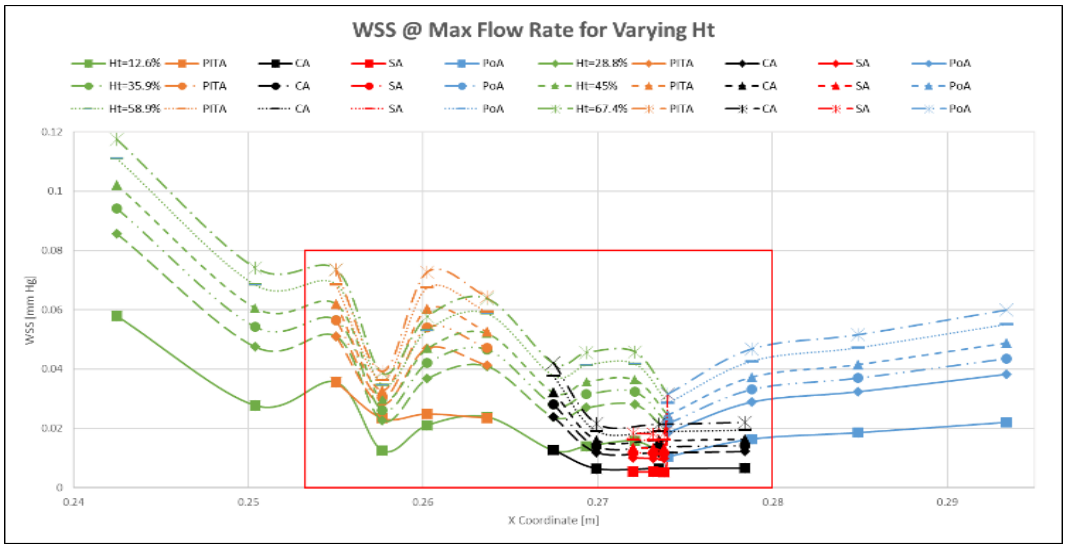

Fig. 17: Wall shear stress for various hematocrits at a flow time 0.1465 (max flow rate). WSS, wall shear stress; Ht, hematocrit; PITA, posterior inferior temporal artery; CA, calcarine artery; SA, splenial artery; PoA, parieto-occipital artery

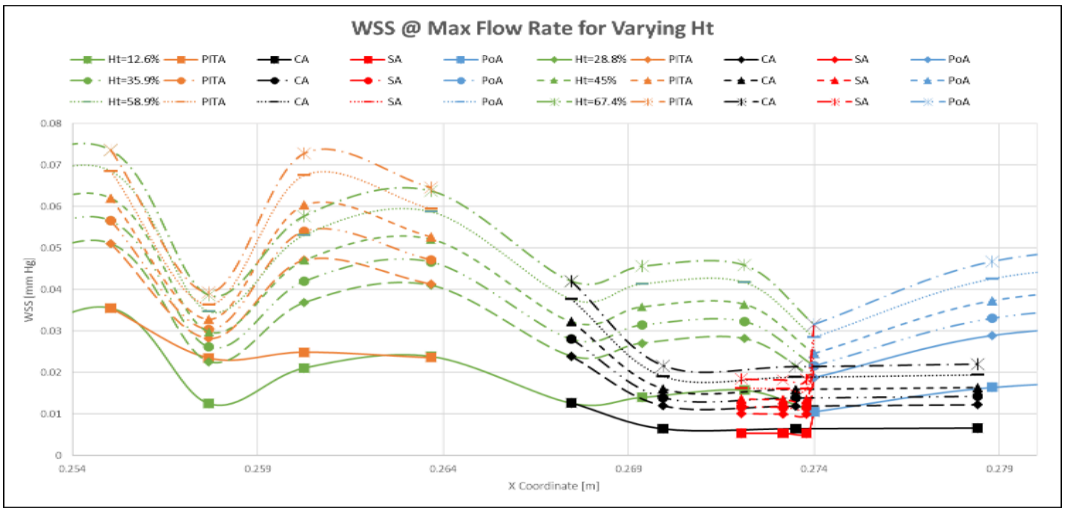

Fig. 18: Zoomed-in red rectangle portion of Fig. 17. WSS, wall shear stress; Ht, hematocrit; PITA, posterior inferior temporal artery; CA, calcarine artery; SA, splenial artery; PoA, parieto-occipital artery

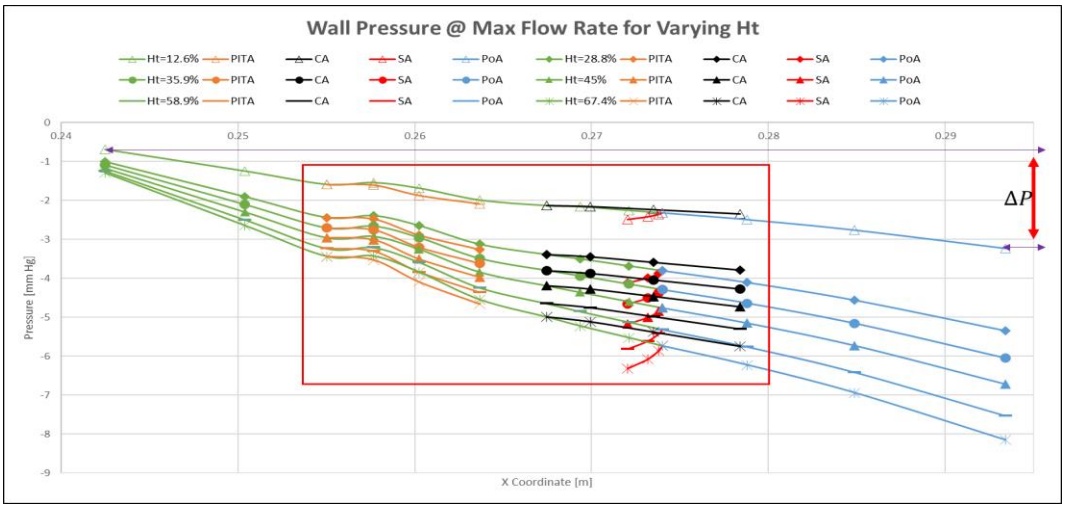

Fig. 19: Wall pressure for various hematocrits at flow time (max flow rate). Ht, hematocrit; PITA, posterior inferior temporal artery; CA, calcarine artery; SA, splenial artery; PoA, parieto-occipital artery

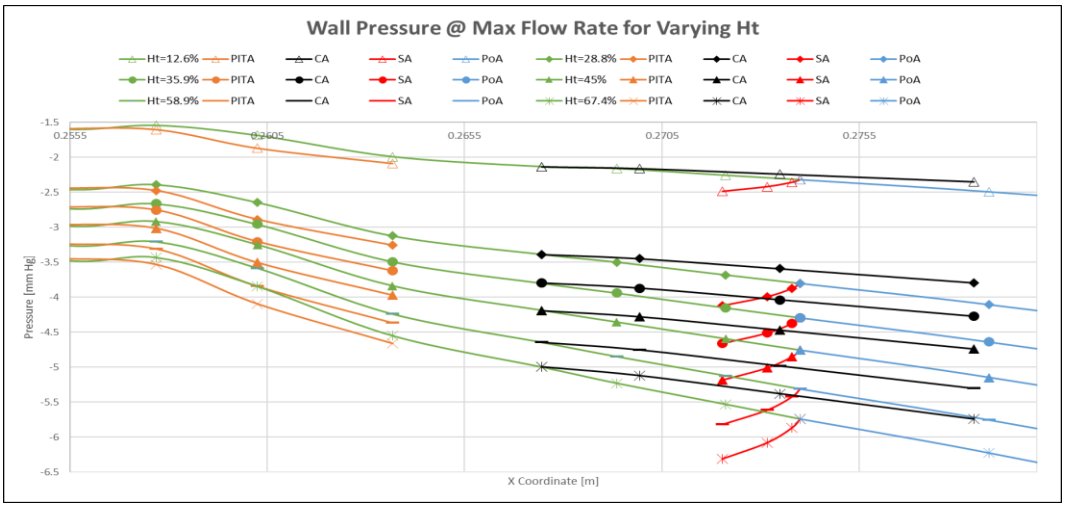

Fig. 20: Zoomed-in red rectangle portion of Fig. 19. Ht, hematocrit; PITA, posterior inferior temporal artery; CA, calcarine artery; SA, splenial artery; PoA, parieto-occipital artery

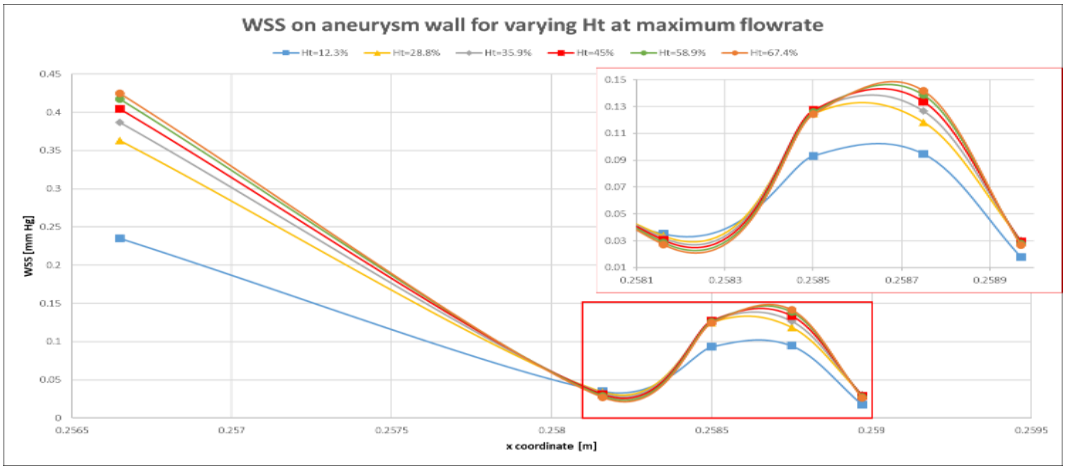

Fig. 21: Wall shear stress at the aneurysm site for various hematocrits at flow time (max flow rate). WSS, wall shear stress; Ht, hematocrit

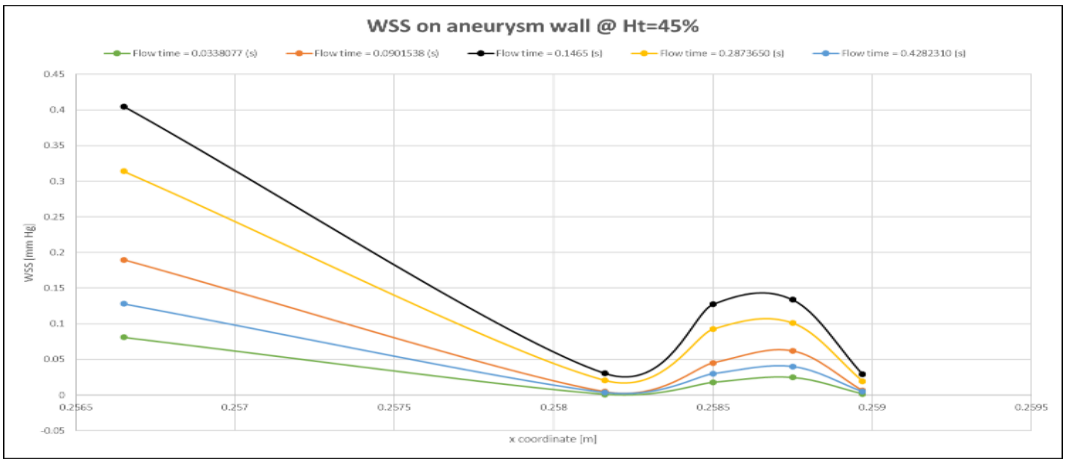

Fig. 22: Wall shear stress at the aneurysm site for various flow rates at hematocrit. WSS, wall shear stress; Ht, hematocrit

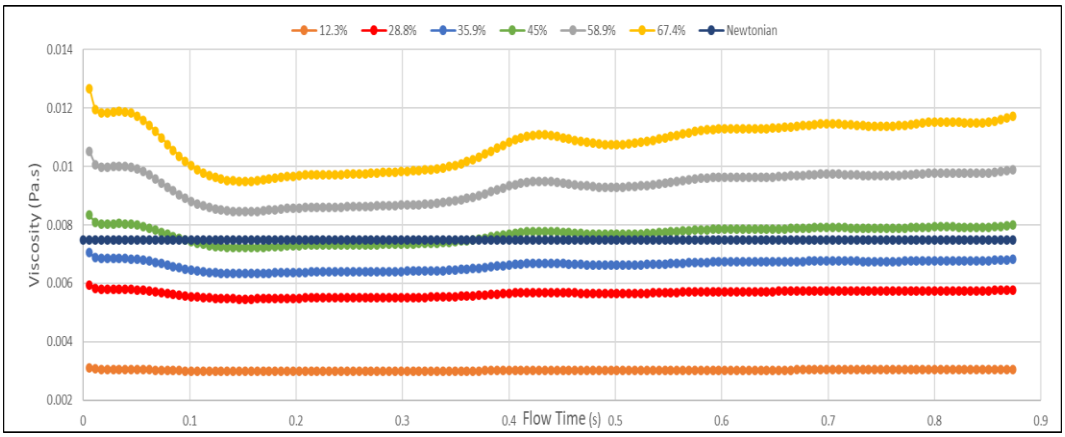

Fig. 23. Area-weighted average viscosity against flow time for various hematorcit concentrations

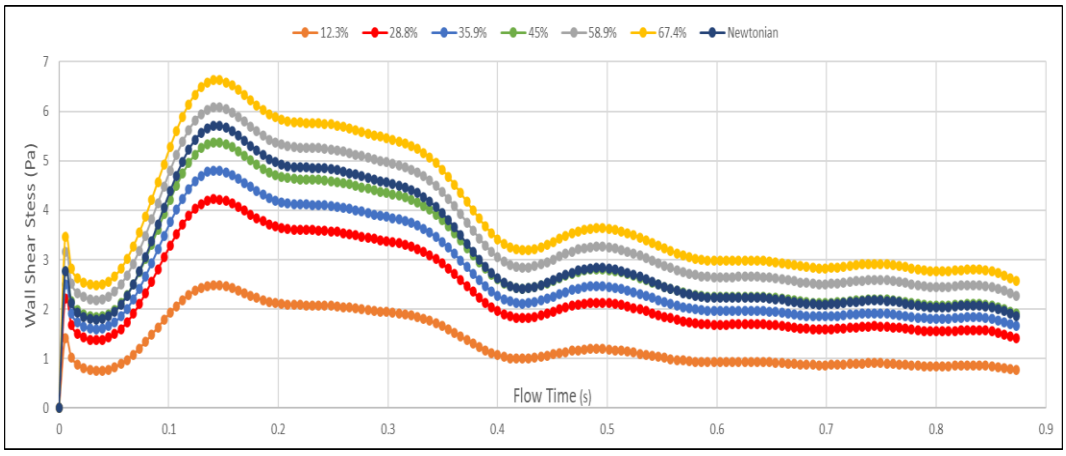

Fig. 24. Area-weighted average wall shear stress against flow time for various viscosity models

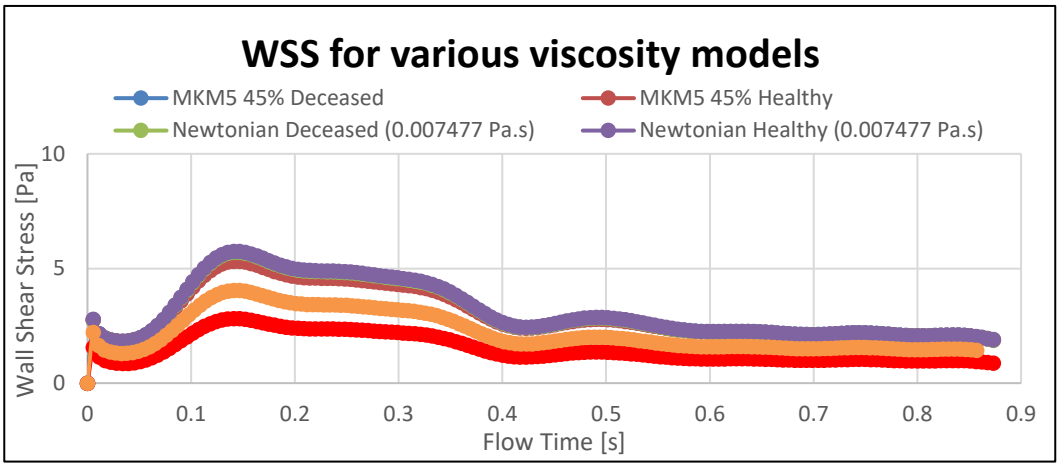

Fig. 25. Area-weighted average wall shear stress against flow time for healthy Vs diseased geometries. WSS, wall shear stress; MKM5, modified Krieger model 5

4. CONCLUSIONS

The effects of the hematocrit variation on the wall pressure and the WSS of the P2P segment of PCA with an aneurysm were considered. The WSS values were found to vary considerably with the hematocrit value; for example, for a hematocrit value of 45%, which was the normal value, the maximum WSS was found to be approximately 5.25 Pa. Similarly, for the hematocrit value of 12.3%, the maximum WSS was approximately 2.5 Pa with a decrease of approximately 52%. For a hematocrit value of 67.4%, the maximum WSS was 6.5 Pa with an increase of about 24%. This study provides a mechanistic insight, demonstrating computationally that low hematocrit reduces wall shear stress (WSS), a key driver of aneurysm wall remodeling. This suggests a potential hemodynamic link where anemia could increase rupture risk. However, this link remains hypothetical and must be validated through future clinical and epidemiological studies. If confirmed, it would argue for including hematological profile in comprehensive aneurysm risk assessment. Another important finding from this study that may save computational power for future research is that the Newtonian model can provide results as accurately as those of the complicated shear-thinning MKM5 model for a modified average viscosity value based on the local shear rate range. This research connects hemodynamic and engineering. It allows for cost-effective simulations, safer device designs, and more precise methods for managing aneurysms. Adding AI and wearable sensors could transform care for cerebrovascular issues.

5. REFERENCES

Cebral, J.R., Castro, M.A., Appanaboyina, S., Putman, C.M., Millan, D. and Frangi, A.F., 2005. Efficient pipeline for image-based patient-specific analysis of cerebral aneurysm hemodynamics: technique and sensitivity. IEEE transactions on medical imaging, 24(4), pp.457-467.

Cherry, E.M. and Eaton, J.K. (2013) ‘Shear thinning effects on blood flow in straight and curved tubes’, Physics of Fluids, 25(7), p. 073104. doi:10.1063/1.4816369.

Elakhdar, A., Elhagri, M., Naguib, C. and Elshabrawy, M. (2021) ‘CFD analysis of transient blood flow in a cerebral aneurysm: A comparison between a healthy and diseased model’, 2021 3rd Novel Intelligent and Leading Emerging Sciences Conference (NILES). IEEE.

Elhanafy, A., Elsaid, A. and Guaily, A. (2020) ‘Numerical investigation of hematocrit variation effect on blood flow in an arterial segment with variable stenosis degree’, Journal of Molecular Liquids, 313, p. 113550. doi:10.1016/j.molliq.2020.113550.

Elhanafy, A., Guaily, A. and Elsaid, A. (2019) ‘Numerical simulation of blood flow in abdominal aortic aneurysms: Effects of blood shear-thinning and viscoelastic properties’, Mathematics and Computers in Simulation, 160, pp. 55–71. doi:10.1016/j.matcom.2018.12.006.

Geers, A.J., Morales, H.G., Larrabide, I. and Frangi, A.F. (2017) ‘Comparison of steady-state and transient blood flow simulations of intracranial aneurysms’, Annual International Conference of the IEEE Engineering in Medicine and Biology Society. doi:10.1109/EMBC.2017.8036982.

Hassan, Q.H., Ahmed, S.T. and Mahdi, A.A. (2014) 'Numerical simulation of air velocity and temperature distribution inside a two-dimensional office room.' Kufa Journal of Engineering, 6(1).

Hund, S., Kameneva, M. and Antaki, J. (2017) ‘A quasi-mechanistic mathematical representation for blood viscosity’, Fluids, 2(1), p. 10. doi:10.3390/fluids2010010.

Hwary, A.S.Z., Khalil, E.E., Abohadima, S. and El-Shabrawy, M. (2021) 'Numerical investigation of heat transfer enhancement in double pipe heat exchanger using twisted tape insert', AIAA Scitech 2021 Forum, pp. 1-10.

Issakhov, A. and Abylkassymova, A. (2023a) ‘Numerical analysis of solid barrier heights and trees with porosity properties influence on the automobile’s emission dispersion in the residential area’, Ecological Modelling, 484, p. 110395. doi:10.1016/j.ecolmodel.2023.110395.

Issakhov, A. and Abylkassymova, A. (2023b) ‘Numerical study of the dam-break flood over natural rivers with macroscopic rocks on movable beds’, Computers and Geotechnics, 164, p. 105793. doi:10.1016/j.compgeo.2023.105793.

Kuchumov, A.G. et al. (2022) ‘The effects of the mechanical properties of vascular grafts and an anisotropic hyperelastic aortic model on local hemodynamics during modified Blalock–Taussig shunt operation, assessed using FSI simulation’, Materials, 15(8), p. 2719. doi:10.3390/ma15082719.

Lo, S.C.Y., McCullough, J.W.S. and Coveney, P.V. (2022) 'Parametric analysis of an efficient boundary condition to control outlet flow rates in large arterial networks', Scientific Reports, 12, p. 19092. doi:10.1038/s41598-022-21923-9.

Luo, B. et al. (2011) 'High shear stress and flow velocity in partially occluded aneurysms prone to recanalization', Stroke, 42(3), pp. 745–753. doi:10.1161/STROKEAHA.110.593517.

Meng, H., Wang, Z., Hoi, Y., Gao, L., Metaxa, E., Swartz, D.D. and Kolega, J., 2007. Complex hemodynamics at the apex of an arterial bifurcation induces vascular remodeling resembling cerebral aneurysm initiation. Stroke, 38(6), pp.1924-1931.

Miskdjian, I., Hodhod, H., Abdeen, M. and Elshabrawy, M. (2024) 'Investigation and optimization of factors affecting the accuracy of strain measurement via digital image processing', Journal of Engineering and Applied Science, 71(1), art. no. 63. doi:10.1186/s44147-024-00372-3.

Mohammed, H.A., Kareem, S.W. and Mohammed, A.S. (2022) 'A comparative evaluation of deep learning methods in digital image classification.' Kufa Journal of Engineering, 13(4), pp. 53–69.

Moon, J. et al. (2014) 'Considerations of blood properties, outlet boundary conditions and energy loss approaches in computational fluid dynamics modeling', Neurointervention, 9(1), pp. 1–8. doi:10.5469/neuroint.2014.9.1.1.

Onoroh, F., Ogbonnaya, M. and Agberegha, L.O. (2023) 'Performance evaluation of hot air thermoelectric generator using biomass energy source', Kufa Journal of Engineering, 14(4), pp. 69–85. doi: 10.30572/2018/KJE/140406.

Ostrowski, K. and Tan, J. (2022) 'Direct simulation of blood flow with heterogeneous cell suspensions in a patient-specific capillary network', Physics of Fluids, 34(4), p. 041912. doi:10.1063/5.0086647.

Sakariassen, K., Orning, L. and Turitto, V. (2015) 'The impact of blood shear rate on arterial thrombus formation', Future Science OA, 1(4). doi:10.4155/fso.15.28.

Salvi, P., Bellasi, A. and Di Iorio, B. (2013) 'Does it make sense to measure only the brachial blood pressure?', Blood Purification, 36(1), pp. 21–25. doi:10.1159/000350581.

Sforza, D.M., Putman, C.M. and Cebral, J.R., 2009. Hemodynamics of cerebral aneurysms. Annual review of fluid mechanics, 41(1), pp.91-107.

Shimogonya, Y. and Fukuda, S. (2024) 'Role of disturbed wall shear stress in the development of cerebral aneurysms', Journal of Biomechanics, 176, p. 112355. doi:10.1016/j.jbiomech.2024.112355.

Souza, A., Lopes, D., Souza, S., Ribeiro, J., Lima, R.A. and Ferrera, C., 2024. Experimental and numerical analyses of the hemodynamics impact on real intracranial aneurysms: A particle tracking approach. Results in Engineering, 24, p.103566. https://doi.org/10.1016/j.rineng.2024.103566

Vignali, E. et al. (2021) 'Fully coupled FSI computational analyses in the ascending thoracic aorta using patient-specific conditions and anisotropic material properties', Frontiers in Physiology, 12, p. 732561. doi:10.3389/fphys.2021.732561.

Vignon-Clementel, I., Figueroa, C., Jansen, K. and Taylor, C. (2010) 'Outflow boundary conditions for 3D simulations of non-periodic blood flow and pressure fields in deformable arteries', Computer Methods in Biomechanics and Biomedical Engineering, 13(5), pp. 625–640. doi:10.1080/10255840903413565.

Vu, D.L. et al. (2025) 'Hemodynamic characteristics in ruptured and unruptured intracranial aneurysms: A prospective cohort study utilizing the AneurysmFlow tool', American Journal of Neuroradiology, 46(1), pp. 75–83. doi:10.3174/ajnr.A8444.

Wajihah, S.A. and Sankar, D.S. (2023) 'A review on non-Newtonian fluid models for multi-layered blood rheology in constricted arteries', Archive of Applied Mechanics, 93, pp. 1771–1796. doi:10.1007/s00419-023-02368-6.

Weber, T. et al. (2004) 'Arterial stiffness, wave reflections, and the risk of coronary artery disease', Circulation, 109(2), pp. 184–189. doi:10.1161/01.CIR.0000105767.94169.E3.

World Health Organization (n.d.) cardiovascular diseases. Available at: https://www.who.int/health-topics/cardiovascular-diseases (Accessed: 2 February 2025).

Xiang, J. et al. (2011) 'Hemodynamic–morphologic discriminants for intracranial aneurysm rupture', Stroke, 42(1), pp. 144–152. doi:10.1161/STROKEAHA.110.592923.

Zhou, G. et al. (2020) 'An assessment of how the anterior cerebral artery anatomy impacts ACoA aneurysm formation based on CFD analysis', British Journal of Neurosurgery, 38(2), pp. 215–219. doi:10.1080/02688697.2020.1726285.